SANDIA REPORT
SAND2022-6710
Printed May 2022

Sandia National Laboratories

A study of sacrificial mirrors for use prior to a laser wakefield accelerator driven by the Z-Petawatt laser

LDRD 222434

Benjamin R. Galloway[1], Patrick K. Rambo[1], Matthias Geissel[1], Mark W. Kimmel[1], Jeffrey W. Kellogg[1], Jennifer Elle[2], Travis Garrett[2], John L. Porter[1], Gregory A. Rochau[1]

[1]Sandia National Laboratories, Albuquerque, NM 87185
[2]Air Force Research Laboratory, Kirtland Air Force Base, NM 87117

Prepared by
Sandia National Laboratories
Albuquerque, New Mexico
87185 and Livermore,
California 94550

Issued by Sandia National Laboratories, operated for the United States Department of Energy by National Technology & Engineering Solutions of Sandia, LLC.

Available to DOE and DOE contractors from
U.S. Department of Energy
Office of Scientific and Technical Information
P.O. Box 62
Oak Ridge, TN 37831

Telephone: (865) 576-8401
Facsimile: (865) 576-5728
E-Mail: reports@osti.gov
Online ordering: http://www.osti.gov/scitech

Available to the public from
U.S. Department of Commerce
National Technical Information Service
5301 Shawnee Rd
Alexandria, VA 22312

Telephone: (800) 553-6847
Facsimile: (703) 605-6900
E-Mail: orders@ntis.gov
Online order: https://classic.ntis.gov/help/order-methods/

ABSTRACT

Many experiments at Sandia's Z Pulsed Power Facility require x-ray backlighting diagnostics to understand experiment performance. Due to limitations in present-day source/detection modalities, most x-ray diagnostics at Z are restricted to photon energies <20 keV, ultimately limiting the density, amount, and atomic number of targets diagnosable in experiments. These limitations force the use of low-Z materials like Beryllium, and they prevent acquisition of important backlighting data for materials/densities that are opaque to soft x-rays and where background emission from the Z load and transmission lines overwhelm diagnostics. In this LDRD project, we have investigated the design and development of a laser wakefield acceleration platform driven by the Z-Petawatt laser – a platform that would enable the generation of a pulsed, collimated beam of high energy x-rays up to 100 keV. Geometrical considerations for implementation on the Z Machine require the use of sacrificial mirrors, which have been tested in offline experiments in the Chama target chamber in building 983. Our results suggest the use of sacrificial mirrors would not necessarily inhibit the laser wakefield x-ray process, particularly with the benefits stemming from planned laser upgrades. These conclusions support the continuation of laser wakefield source research and the development of the necessary infrastructure to deliver the Z-Petawatt laser to the Z center section along the appropriate lines of sight. Ultimately, this new capability will provide unprecedented views through dense states of matter, enabling the use of previously incompatible target materials/designs, and uncovering a new set of observables accessible through diffraction and spectroscopy in the hard x-ray regime. These will amplify the data return on precious Z shots and enhance Sandia's ability to investigate fundamental physics in support of national security.

ACKNOWLEDGEMENTS

The authors express their great appreciation to staff and management for their help and support during this project: Jonathon Shores, Shane Speas, Robert Speas, Ian Smith, and Jeff Kellogg for technical advice and support for facility matters and engineering; Patrick Knapp, Richard Harrison, Kyle Thompson, and Amber Dagel for their expertise and guidance regarding applications of the laser wakefield x-ray source; John Porter, Greg Rochau, Dan Sinars, Chris Seagle, and Luke Shulenberger for their support of this project and advocating for its success.

We also thank our collaborators at the Air Force Research Labs for their expert guidance and participation in target design and simulation work for the laser wakefield acceleration platform: Jennifer Elle and Travis Garrett.

This work was sponsored by the Laboratory Directed Research and Development (LDRD) Program at Sandia National Laboratories.

CONTENTS

LIST OF FIGURES

LIST OF TABLES

ACRONYMS AND DEFINITIONS

Abbreviation	Definition
LWFA	Laser Wakefield Acceleration
ICS	Inverse Compton Scattering
SM	Sacrificial Mirror
PM	Plasma Mirror
ZPW	Z-Petawatt Laser
TRL	Technical Readiness Level
FOA	Final Optics Assembly
LDRD	Laboratory Directed Research and Development
LIDT	Laser Induced Damage Threshold
TNSA	Target Normal Sheath Acceleration

1. EXECUTIVE SUMMARY

1.1. Purpose

Many experiments at Sandia's Z Facility require x-ray backlighting diagnostics to understand experiment performance. Due to limitations in present-day source/detection modalities, most x-ray diagnostics at Z are restricted to photon energies <20 keV, ultimately limiting the density, amount, and atomic number of targets diagnosable in experiments. These limitations force the use of low-Z materials like Beryllium, and they prevent acquisition of important backlighting data for materials/densities that are opaque to soft x-rays and where background emission from the Z pulsed power environment overwhelms diagnostics.

To fill this critical gap in x-ray diagnostics at Z, this project aims to develop a hard x-ray source generated by the Laser Wakefield Acceleration (LWFA) process. Published efforts in LWFA demonstrate this source to be pulsed (<1 ps duration), highly directional (~100 mrad divergence), and capable of generating x-rays >100 keV when driven by a laser like the Z-Petawatt (ZPW) short-pulse laser [1,2] (see Figure 1-1). Signal-to-noise ratios can be high through efficient use of the directional beam, the high transmission of hard x-rays, and strong spectral filtering of the <20 keV background from Z. Thicker filters also add to detector's debris-resistance, as demonstrated on Z with Compact Point-Projection System (C-PoPS). The laser-like output enables large-standoff, optics-free diagnostic techniques like phase contrast imaging [3,4,5] (lending advantages in radiography), and dynamic Laue diffraction [6,7] (benefitting efforts in dynamic materials properties).

Success in this project will deliver a game-changing diagnostic capability to the Z Facility, providing an unprecedented view through dense objects, enabling the use of previously incompatible target materials/designs, and uncovering a new set of observables accessible through diffraction and spectroscopy in the hard x-ray regime. These will enhance the Z Facility's ability to contribute to the NNSA's mission in maintaining the stockpile and to investigate fundamental physics in support of national security.

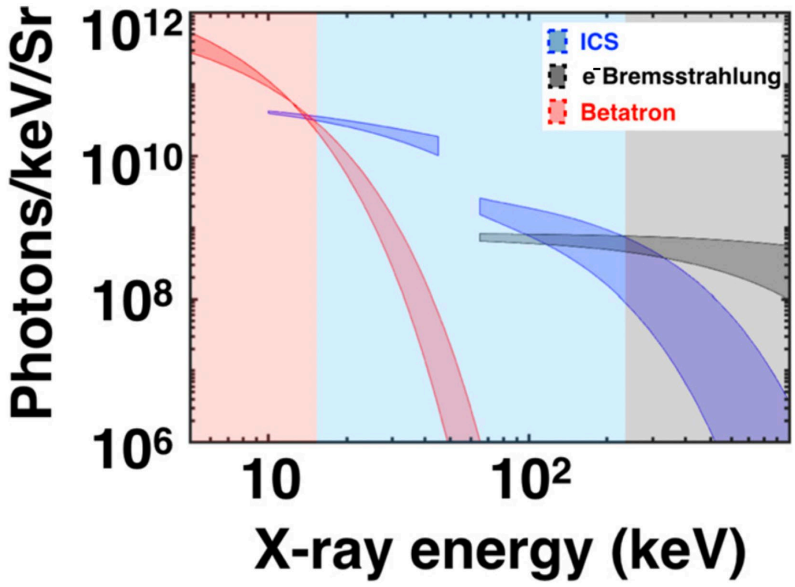

Figure 1-1. X-ray spectra resulting from three LWFA-driven mechanisms, demonstrating usable fluences at photon energies in the tens or hundreds of keV. ICS stands for Inverse Compton Scattering. Background shading colors reflect the dominant mechanisms. Reprinted from [2].

1.2. Goals

Establishing a LWFA platform on the Z Facility is the goal of this effort, with the LDRD project serving to transition the capability from a low Technical Readiness Level (TRL) to moderate TRLs, thereby eliminating much of the uncertainty and scientific risk associated with the development of this new capability based on complex and relatively modern laser physics. Ideally, by the end of the LDRD project, confident statements can be made regarding the feasibility of generating a sufficiently bright and reliable hard x-ray source via ZPW-driven LWFA for diagnostic applications in the Z environment.

1.3. Approach and Summary of Results

The ZPW laser can enter the Z center section through the ZPW Final Optics Assembly (FOA). The ZPW FOA has motorized stages that allow for flexible beam pointing and focusing within a 3-dimensional volume around the Z load. Engineering models of the ZPW FOA and Z center section were analyzed to determine the pointing options available for the LWFA application. For a horizontally-propagating LWFA x-ray beam, the ZPW driving laser must be redirected inside the center section by one or more mirrors. These mirrors will be unavoidably damaged by the laser fluences on their surface and will therefore be considered Sacrificial Mirrors (SM). As ZPW interacts with these SMs, the first portion of the ZPW pulse creates a super-critical density plasma on the SM surface that acts as an efficient reflector for the remainder of the ZPW pulse. There will be energy loss as part of this process and possibly some modulation to the ZPW wavefront, both issues that could affect the subsequent LWFA stage. As such, an investigation into the reflected laser quality from SMs was warranted. In FY21, three experimental campaigns were performed in the Chama target chamber to assess the ZPW laser quality after reflection from SMs and to evaluate the ability for the reflected pulse to drive a nonlinear process in a laser target that demands high intensities. The results from these campaigns suggest high intensity interactions like LWFA can still be performed by ZPW, even after a reflection by a SM. Further, it may be possible to implement ellipsoidal SMs to modify the reflected f/# of ZPW before the LWFA stage, but preliminary results suggest that precise alignment and high-quality ellipsoids are necessary to prevent substantial aberrations upon reflection.

2. PROJECT MANAGEMENT

2.1. Scope of Work

The original proposal for the LDRD project laid out a plan to immediately begin developing the LWFA source in the Chama target chamber (FY21), to optimize the electron and x-ray outputs (FY22), and to pursue proof-of-principle diagnostic applications using the optimized LWFA source (FY23). Due to funding limitations and the uncertainty associated with the use of SMs prior to the LWFA stage (required for use in the Z center section), the scope of work was changed for the awarded LDRD project. A year of investigation into the reflected laser quality from SMs was inserted at the beginning of the original proposal, with the remainder of the plan delayed by one year. As such, the diagnostic applications originally scheduled for year 3 of the LDRD would then need to occur after the LDRD project, requiring the project to be picked up programmatically. Nevertheless, success in the LDRD would help transition the LWFA capability from low TRLs to moderate TRLs while providing secondary benefits to the facility: new infrastructure (gas target capabilities on the Chama target chamber), a deeper understanding of SMs that enable new beam routing options (both in Chama and in the Z center section), and functional Computer-Aided Design (CAD) models of the ZPW FOA.

2.2. Project Schedule and Milestones

Accounting for the change of scope to the LDRD project plan, the milestones and deliverables are listed below:

FY21: SM Investigation

1. Develop CAD models for ZPW LWFA implementation in the Z center section with SMs
    a. Functionalize existing CAD models of the ZPW FOA to allow digital beam steering
    b. Determine beam routing options (mirror placements/angles) for horizontally-propagating LWFA x-rays
2. Perform ZPW shots on flat SMs in the Chama chamber
    a. Measure the reflected laser parameters following flat SMs
    b. Perform Particle-In-Cell (PIC) simulations to evaluate whether experimentally measured aberrations would prohibitively impact a subsequent LWFA stage
    c. Perform solid-target experiments with and without SMs to confirm that the reflected laser quality still results in a high intensity interaction
3. Perform ZPW shots on ellipsoidal SMs in the Chama chamber
    a. Develop mounting fixtures and offline alignment procedures for ellipsoidal SMs
    b. Measure the reflected laser parameters following ellipsoidal SMs
    c. Work toward a publication on the use of ellipsoidal SMs to facilitate long f/# LWFA

FY22: LWFA Platform Development

1. Develop LWFA targets (design, procure, test)
    a. Pulsed gas jet
    b. Pulsed gas cell

2. Develop LWFA diagnostics (design, procure, test)
    a. Electron spectrometer
    b. X-ray spectrometer
    c. Plasma interferometer
    d. Forward spectrometer
3. Perform first LWFA shots
    a. Targets and diagnostics could be tested at the PHEENIX laser (accessible via AFRL collaborators)
    b. Observe LWFA outputs on full ZPW shots in the Chama target chamber without the use of SMs (stretch goal would be to do so while implementing SMs)

FY23: LWFA Optimization

1. Improve the ZPW laser quality deliverable to the Chama target chamber (energy, wavefront, pulse duration, pulse contrast)
2. Perform laser and target parameter scans while measuring outputs to locate the optimal operating space
3. Implement ellipsoidal SMs to drive longer f/# LWFA; perform parameter scans and quantify any gains in output characteristics resulting from the use of ellipsoidal SMs
4. Evaluate LWFA x-ray photometrics compared to background levels in the Z center section to determine whether diagnostic applications will have sufficient signal/background ratios

Post-LDRD: Proof-of-Principle LWFA Applications

1. Using filtering relevant to applications on Z, apply the LWFA x-ray output
    a. to phase contrast radiography of a structured, high-Z sample
    b. to Laue diffraction of a static, high-Z crystal sample
    c. to x-ray spectroscopies of static samples
2. Apply the LWFA electron output to electron radiography of static magnetic fields

Figure 2-1 shows the final project timeline for FY21, accounting for various delays that arose from the dependency of this project on shared facility resources. Figure 2-2 shows the initial project timeline for FY22 before the project was closed in January 2022 due to the principal investigator transitioning away from Sandia.

Task/Milestone	Oct '20	Nov '20	Dec '20	Jan '21	Feb '21	Mar '21	Apr '21	May '21	Jun '21	Jul '21	Aug '21	Sep '21
CAD Designs for Z [1]												
Procurement [2,3]												
Diagnostic Setup [2,3]												
Chamber Setup [2,3]												
Shots: Flat PMs [2a]												
Shots: Solid Targets [2c]												
Shots: Ellipsoids [3b]												
Offline Alignment Procedures [3a]												
LWFA/PM Simulations [2b]												
Coordinate LWFA Runs at Collaborator Facilities												
Publication [3c]												

Figure 2-1. Project timeline for LDRD FY21 (final). Cell color indicates task priority: high (green), medium (yellow), and low (white).

Task/Milestone	Oct '21	Nov '21	Dec '21	Jan '22	Feb '22	Mar '22	Apr '22	May '22	Jun '22	Jul '22	Aug '22	Sep '22
Design gas jet/cell hardware [1]												
Design diagnostic hardware [2]												
Procurement [1,2]												
Assemble and test gas jet/cell hardware [1]												
Assemble and test diagnostics [2]												
Shots: PHEENIX [3a]												
Shots: Chama [3b]												
STRETCH: Chama shots w/ sacrificial mirrors [3b]												
Conference												

Figure 2-2. Project timeline for LDRD FY22 (initial). Cell color indicates task priority: high (green), medium (yellow), and low (white).

3. SACRIFICIAL MIRROR INVESTIGATION

3.1. Reflected Laser Characterization Experiments

To evaluate whether the ZPW laser would be able to drive LWFA after reflecting from a SM, the reflected laser characteristics can be measured on full system shots. The challenge in doing so, however, is that the detectors used to measure the laser cannot handle the full energy or intensity of the reflected laser light. While ZPW would deliver >100 J of energy to the SM, the energy incident on energy meters, cameras, wavefront sensors, and photodiodes must be reduced by several orders of magnitude to avoid damage to the detectors. Further, the measurements must be designed to provide an indication of laser quality, so the optical system between the SM and the detectors should be designed with low aberration and provide imaging relay planes for the laser near-field and far-field. These considerations are necessary for both types of SM to be evaluated (flat and ellipsoidal).

3.1.1. Experiment Design

The reflected laser characterization experiments can be broken up into three components:

1. the SM target(s) inside the Chama chamber
2. the optical system to propagate the reflected laser from the SM(s) to the diagnostic breadboard while satisfying relay imaging conditions and reducing the laser energy to a non-damaging level
3. the diagnostic breadboard that contains various detectors to evaluate laser parameters, including an energy meter, near-field and far-field cameras, wavefront sensor, and cascaded photodiodes to measure pulse contrast.

For flat SMs, the first component is simply the placement of a high-reflecting mirror (dielectric- or silver-coated) in a configuration representative of the intended implementation in the Z center section. Based on the CAD models developed for routing ZPW in the Z center section, flat SMs would be placed 5 inches upstream from the focusing optic's focal point, and the angle of incidence on the SM would range from 30° to 56° depending on the specific line of sight desired within the Z center section (see Figure 3-1). In the case of Z, the SM reflected beam would continue toward focus, where the LWFA gas target would be positioned. In the Chama chamber surrogate case, following reflection from the SM, the ZPW beam would go through focus and would then need to be collected and transported (component 2) to the diagnostics outside of the Chama target chamber (component 3).

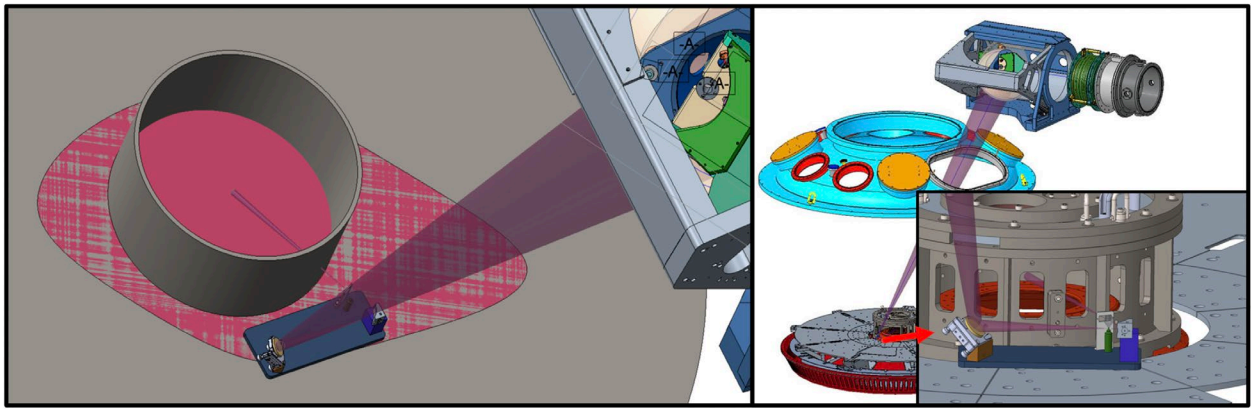

Figure 3-1. CAD model of the Z center section, ZPW Final Optics Aperture, and the beam routing of ZPW using a flat SM and ellipsoidal SM. These models were used to determine the incidence angles of ZPW on SMs and ZPW's full range of pointability (shown as pink area in left image).

The second component of the experimental apparatus in Chama begins following the focal point of the reflected beam. To allow for imaging diagnostics as well as capture the full beam that diverges strongly following the focus, a collection lens is required. Due to the high fluences and intensities that are present in these experiments, the beam energy is reduced by taking reflections from a series of two 4 in. x 8 in. wedges prior to collection by a 6 in. diameter lens. Mirrors then transport the beam outside the Chama target chamber and to a diagnostic breadboard. During its propagation, the beam size gradually decreases after the 6 in. diameter lens. Before reaching the diagnostic breadboard, the beam passes through a pair of lenses (one positive and one negative) that help to compensate for optical aberrations induced by the 6 in. diameter lens. Ideally, this optical transport system would not induce any aberrations to the beam such that the diagnostics could then measure a beam representative of what immediately follows the SM. However, this was found to be challenging to realistically implement, so a best effort approach was pursued to minimize aberrations as much as practical. Figure 3-2 shows a CAD model of the optical layout in the Chama target chamber through to the beginning of the diagnostic breadboard.

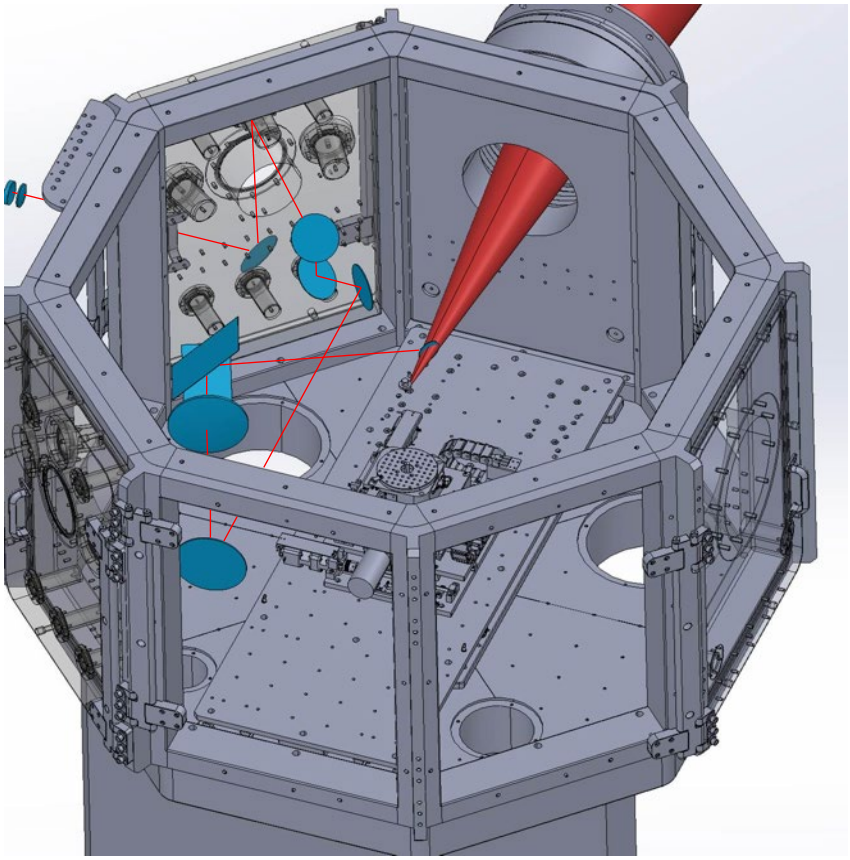

Figure 3-2. CAD model of the Chama target chamber and optical layout to propagate the reflected ZPW beam to the diagnostic breadboard (offscreen to left). The ZPW input is shown as a red cone, while only the centerline is shown following the SM. Optics are shown in blue.

The final component of the experimental apparatus is the diagnostic breadboard that splits the beam into multiple copies to then be measured by a suite of different diagnostics. These diagnostics include an energy meter, wavefront sensor, near-field camera, far-field camera, and a set of photodiodes to measure pulse contrast. The beam splitting is performed in such a way to induce the fewest aberrations

for those diagnostics that are sensitive to aberrations: the wavefront sensor and far field camera. Because the optical transport and imaging system prior to the diagnostics induce a nonzero amount of aberration, what is measured by the wavefront sensor and far field camera will not be a perfect representation of the focusability of the beam immediately after reflecting from the SM. As such, the information that can be gained from these diagnostics lies in how the wavefront changes from pre-shot to on-shot. When considering the focusing ZPW laser, the presence of the SM before the focus should not degrade the beam's wavefront and focusability if the SM is originally flat and not actually damaged on the shot (i.e. at low fluence levels as with an alignment beam). Therefore, it can be assumed that a pre-shot measurement with the low-level ZPW seed would represent a baseline for an optimally-focused beam after reflecting from the high-reflector that will later serve as the SM on-shot. By comparing the on-shot wavefront and far-field measurements to the pre-shot measurements, one can infer what the actual focus inside the Chama chamber must have been after reflecting from (and damaging) the SM. This scheme can therefore overcome the limitations of using a non-ideal optical transport system that imparts aberration to the beam. As for the energy and pulse contrast measurements, neither of these diagnostics are sensitive to aberration. Beams that transmit through wedges are allowed, and a negative lens is used in the energy meter beam path to achieve a large enough spot size on the meter head. Figure 3-3 shows the full diagnostic breadboard layout, including the set of four photodiodes that are sensitive to varying ranges of amplitude levels that can then be used to construct a high dynamic range measurement of nanosecond-scale pulse contrast. It is noted that despite the two wedges used to reduce the beam energy delivered to the diagnostic breadboard, intensity levels can still be high enough to cause self-focusing effects in wedges or in air at a focus. This problem was found to cause erroneous results in previous iterations of the diagnostic layout where small beam sizes or foci existed in the wavefront sensor and energy meter beam paths.

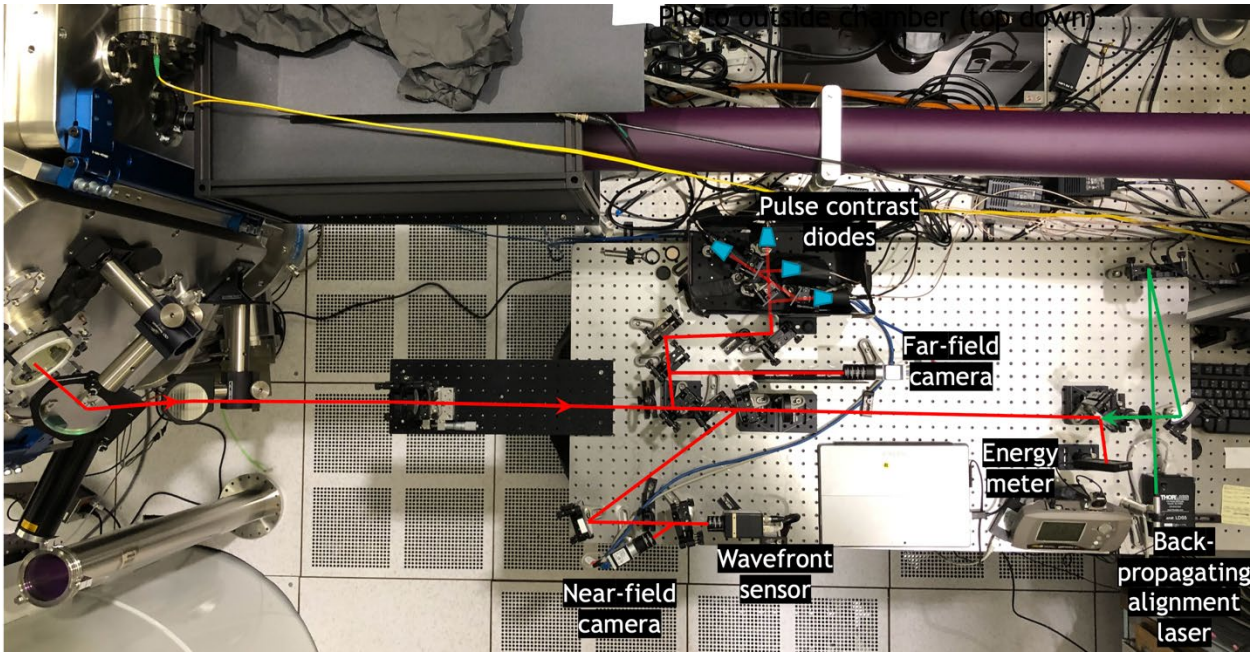

Figure 3-3. Top-down photo of the diagnostic breadboard for SM experiments. The apparatus begins with an outrigger supporting the positive and negative lenses that reduce aberrations and adjust the far-field plane. Wedges are used to split the beam to the various detectors. A negative lens is placed along the energy meter beam path, and a positive lens is placed prior to the near-field and wavefront diagnostics to produce a collimated, imaged near-field. The pulse contrast photodiodes use wedges to produce successively weaker signals until the final photodiode measures the full pulse without saturation.

The mirrors used in the flat SM campaign were of two types: protected silver mirrors and dielectric high reflector mirrors designed for 1054 nm. The laser induced damage threshold (LIDT) for dielectric mirrors is typically higher than that of metal mirrors, so exploring any differences between these two types of SM was of interest. Because of the placement and angle of incidence for these experiments, it was necessary to use 2 in. diameter mirrors to accommodate the full beam projection without clipping. Much of the in-chamber optical apparatus was assembled with kinematic mounts to allow for rapid SM replacement and alignment between shots. Kinematic mounts were particularly instrumental for alignment of the 4 in. x 8 in. wedges, where silver-coated versions were used for preliminary alignment using IR viewers and IR cards, and then each wedge was sequentially replaced with uncoated versions while maintaining near-field and far-field profiles on the diagnostic cameras.

In addition to the flat SMs described above, ellipsoidal SMs were also investigated. In LWFA, theory indicates that there are optimal laser and plasma parameters to drive the process efficiently and with high output fluence. It is important to deliver input laser parameters (i.e. focal spot size) that correlate to the plasma parameters (i.e. plasma wavelength). For the Z-Petawatt energy and pulse duration, theory would suggest driving with longer f/# focusing optics to create larger focal spot widths would benefit the LWFA process. As such, a campaign was performed to investigate ellipsoidal SMs very similarly to the flat SM campaign but using a slightly modified apparatus to account for the differences between flats and ellipsoids.

It was desired to leave the optical transport and diagnostic components of the setup relatively unchanged to make use of the same optics and make relevant comparisons between the results. For this to be accomplished, it was necessary to use a pair of ellipsoids placed after the ZPW focus in Chama such that the incoming and outgoing beam divergence was maintained, just as is the case for flat SMs. This ensured that the beam sizes on each of the optics would not be too large to clip or too small to cause nonlinear phenomena on/in transport optics. A small breadboard was used to mount the ellipsoids and precisely align them using a surrogate alignment beam (see Figure 3-4 for a photo of the breadboarded ellipsoid pair system). The breadboard was then installed into the Chama target chamber and aligned to the ZPW input beam (see Figure 3-5 for the Zemax layout of the transport optics for the ellipsoidal SM case). Protected gold ellipsoids were used with either 2 or 2.5 times magnification (between ellipsoid foci), representing the same increase or decrease in f/# achievable when using such ellipsoids.

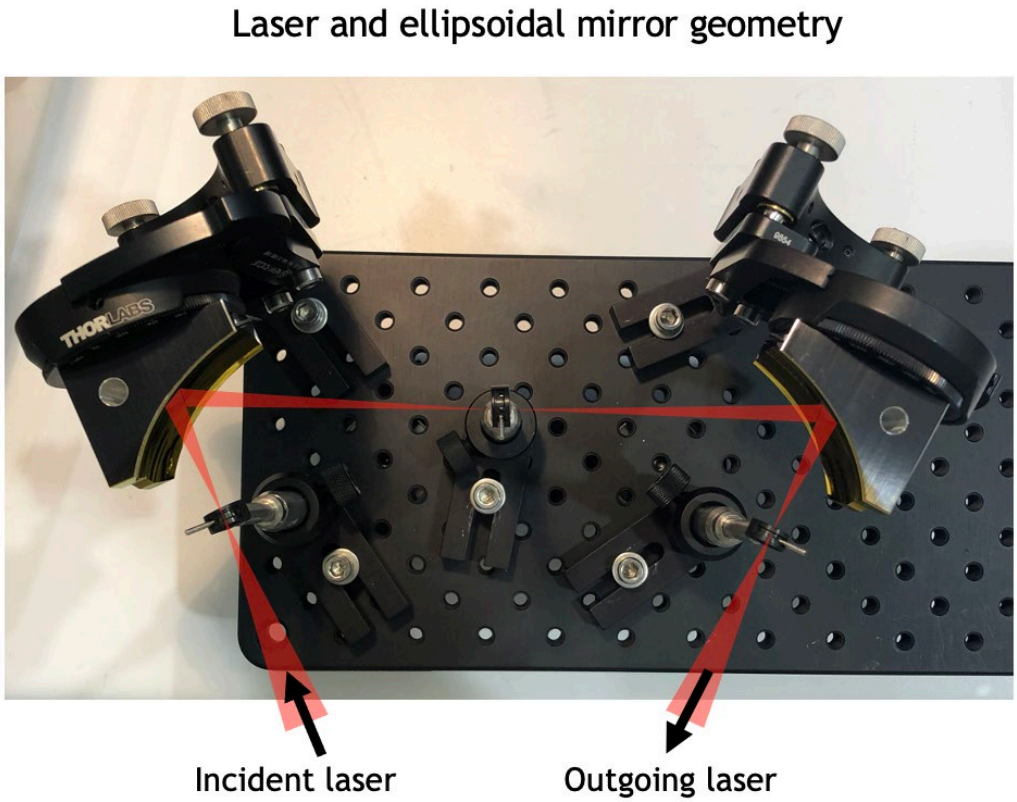

Figure 3-4. A custom breadboard and optomechanical system used to allow for offline alignment of the ellipsoid pair prior to installation into the Chama target chamber.

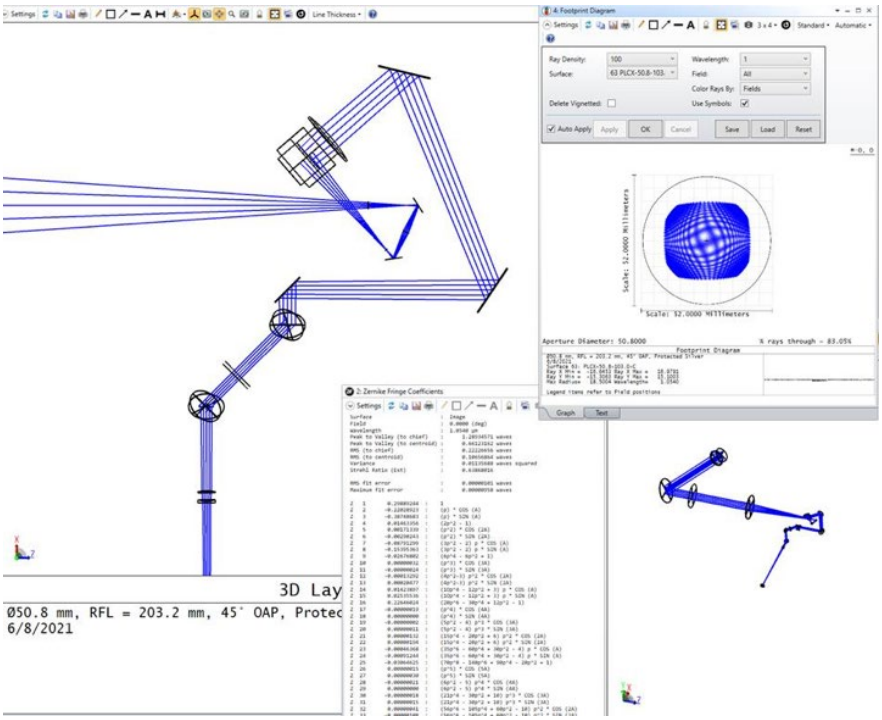

Figure 3-5. A Zemax screenshot showing the optical layout for the ellipsoid pair system and the subsequent optical transport system to deliver the beam to the diagnostic breadboard. In the upper left window, the ZPW input enters from the left and the diagnostic breadboard is toward the bottom.

3.1.2. Experimental Results

A total of 22 shots were performed using flat SMs, while 8 shots were performed using ellipsoidal SMs. Shot energies started low to tune diagnostic parameters and obtain baseline results in a regime where fluences and intensities would not be high enough to cause nonlinear effects in the diagnostic beam paths. As shot energies increased, it was discovered that surface ionization on wedges or nonlinear self-focusing within the diagnostic system (at foci or in wedges) had produced erroneous results for a portion of the diagnostic set. Following these discoveries, the diagnostic system was modified to prevent the most susceptible issues and allow for higher energy shots to be performed without erroneous measurements. While this proved successful for the flat SMs, unacceptably high intensities on the first 4 in. x 8 in. wedge were a common and unavoidable problem when using ellipsoidal SMs at ZPW energies above 10 J. It is suspected that the beam reflected from the ellipsoids contains significant intensity modulation resulting from imperfect alignment or insufficient surface topography/polish specification for this application.

The flat SM results are presented as follows:

- Figure 3-6 shows post-shot photos of a protected-silver SM and a dielectric SM at high incidence energy.
- Figure 3-7 summarizes the SM reflectance for each of the shots of the campaign, including the shots with erroneous results from nonlinear effects in the transport/diagnostic beamline. Higher reflectances are observed at higher incidence energies.
- Figure 3-8 summarizes the aberrations induced by flat SMs (pre-shot aberrations subtracted). See sections 3.2 and 3.3 for further discussion on the implications of these aberrations.
- Figure 3-9 shows the pulse contrast measured for one of the flat SM shots. It is noted that the SM campaign inspired an investigation into the ZPW pulse contrast and identified a set of high amplitude pre-pulses that were subsequently removed.

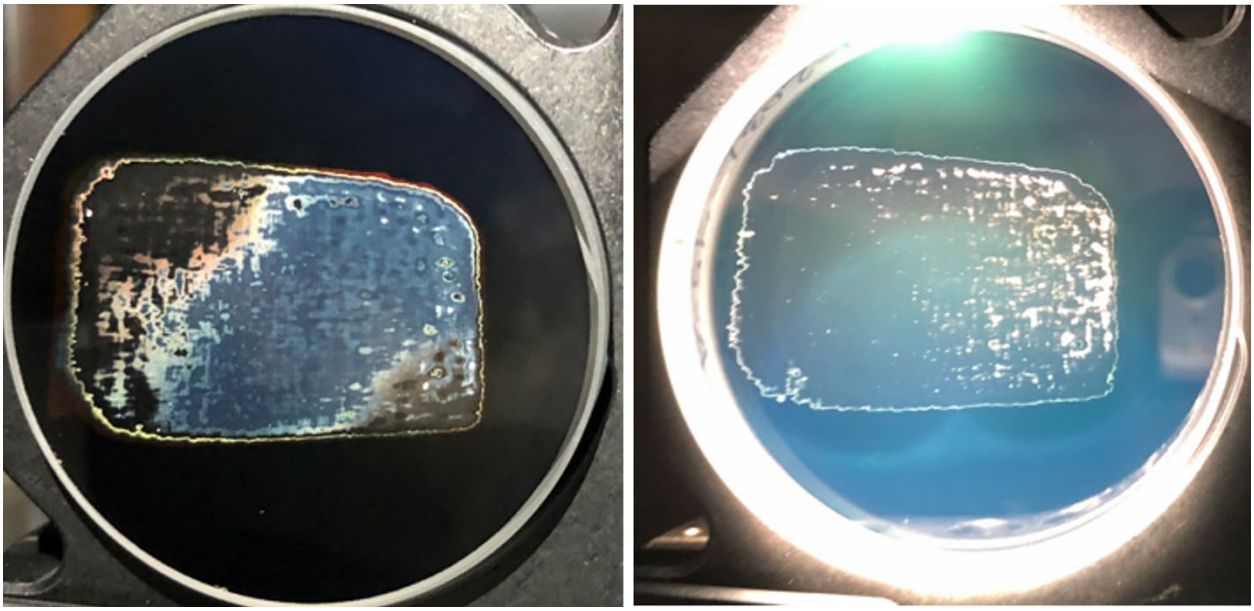

Figure 3-6. Post-shot photos of a silver-coated SM (left) and a dielectric-coated SM (right) using high incidence energy from ZPW. The mirror diameters are 2 inches.

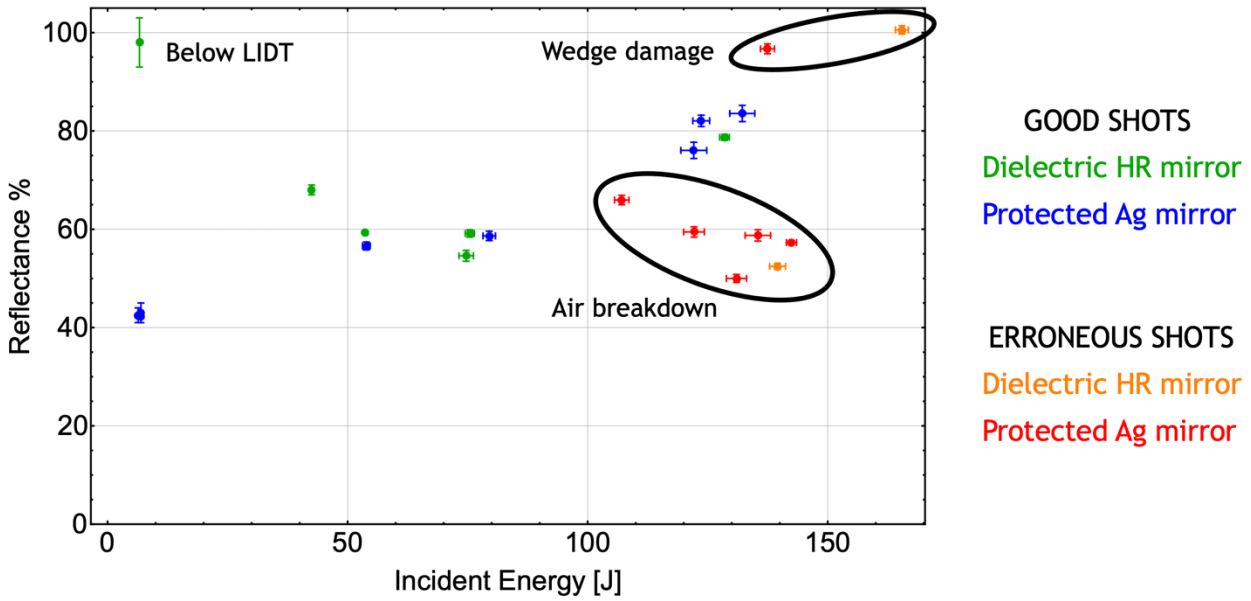

Figure 3-7. Reflectance measurements for all flat SM shots, where nonlinear effects in the relay and diagnostic beam paths caused some shots to produce erroneous results.

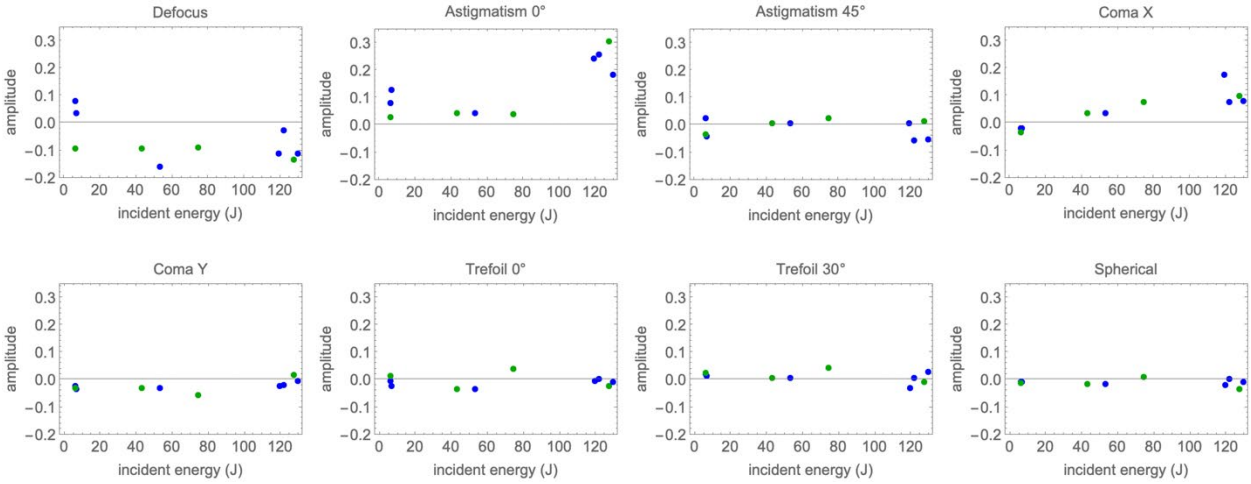

Figure 3-8. Zernike coefficient amplitudes (in waves) representing the aberrations induced on flat SM shots (pre-shot aberrations subtracted). Blue points represent silver-coated SM shots and green points represent dielectric-coated SM shots.

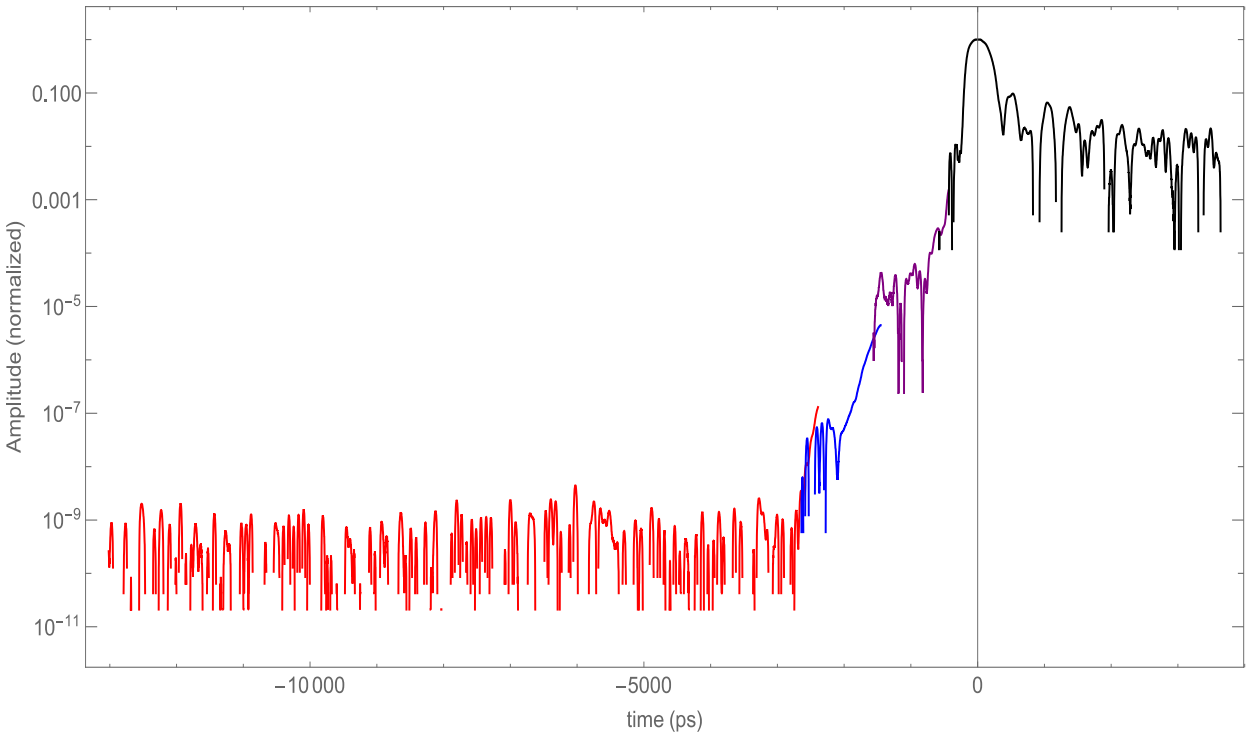

Figure 3-9. Pulse contrast of the ZPW beam reflected by a flat SM, measured by the set of photodiodes. Note that photodiodes used had bandwidths of 5 GHz and 70/110 ps rise/fall times. The different colors represent signals from differently attenuated photodiodes.

The ellipsoidal SM results are presented as follows:

- Figure 3-10 shows on-shot and post-shot images of the ellipsoidal mirror as measured by a color camera mounted outside the chamber.
- Figure 3-11 summarizes the ellipsoidal SM reflectance for each of the shots of the campaign, excluding the shots with erroneous results. The 2x magnification ellipsoids show higher reflectance than the 2.5x magnification ellipsoids, likely due to the smaller beam area on the SM surface.
- Figure 3-12 summarizes the aberrations induced by the ellipsoidal SMs (pre-shot aberrations subtracted).

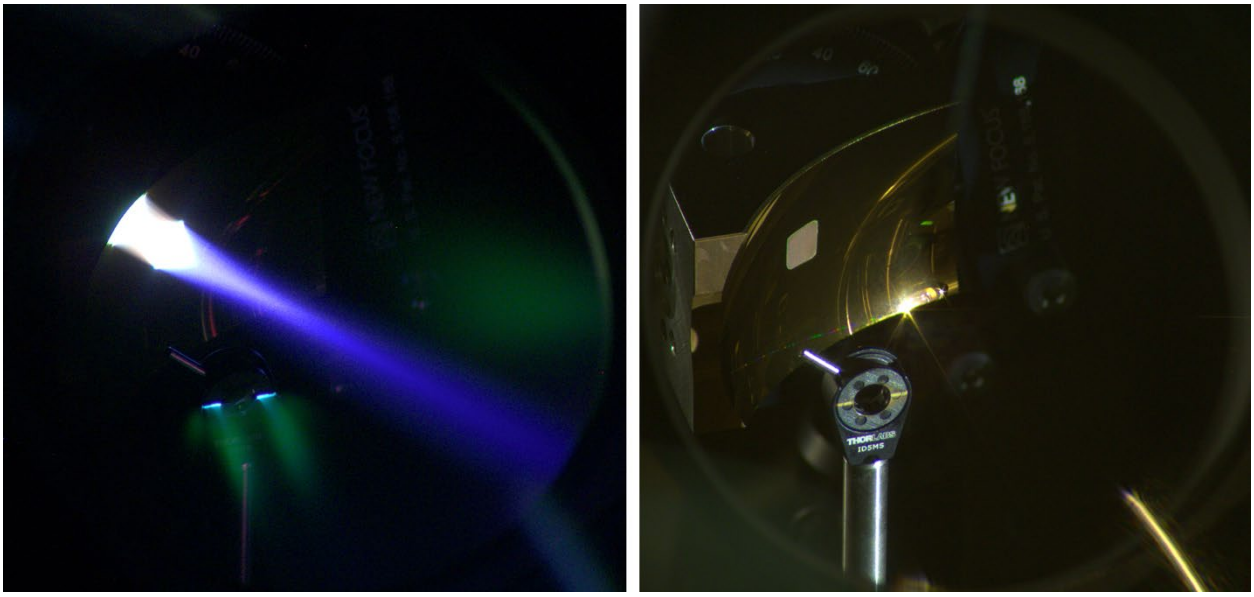

Figure 3-10. On-shot (left) and post-shot (right) images of an ellipsoidal SM, measured by a color camera mounted outside the chamber and imaging with a 4f system. A KG5 step filter was implanted to reduce the amount of ZPW 1054 nm light detected by the camera. The on-shot image shows visible emission from plasma ejected from the ellipsoid surface.

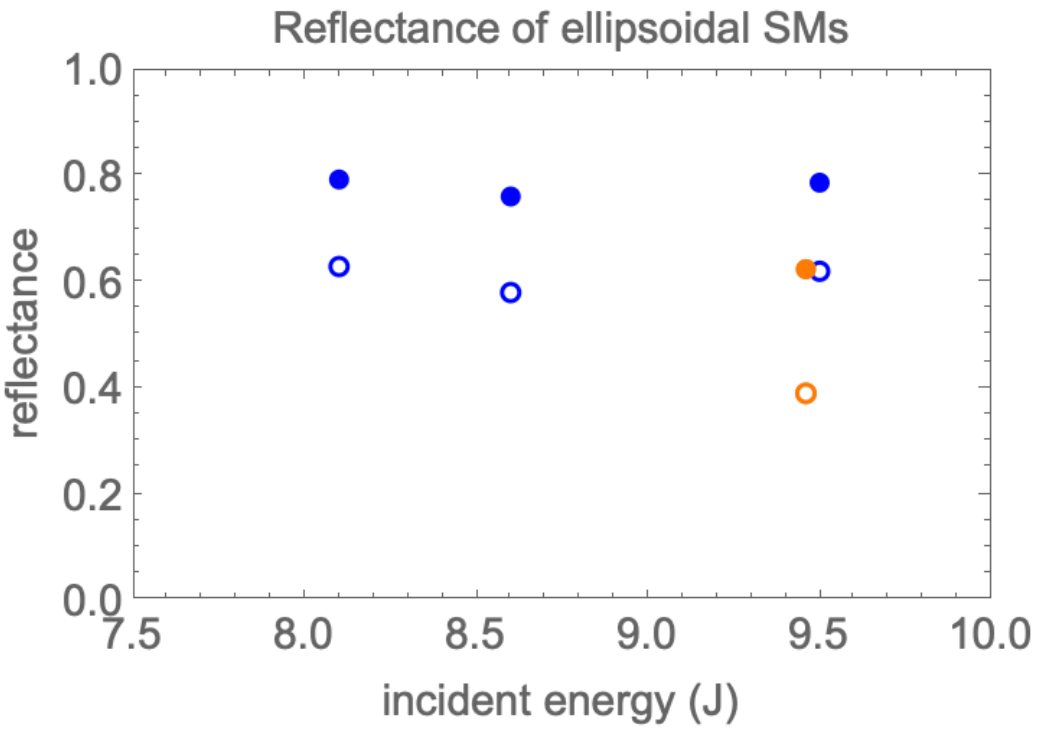

Figure 3-11. Reflectances for ellipsoidal SMs. Open circles represent the reflectance for the pair of ellipsoids (combined, measured), while filled circles represent the reflectance for an individual ellipsoid (assumes equal reflectance from each SM in the pair). Blue points use the 2x magnification ellipsoids while orange points use the 2.5x magnification ellipsoids.

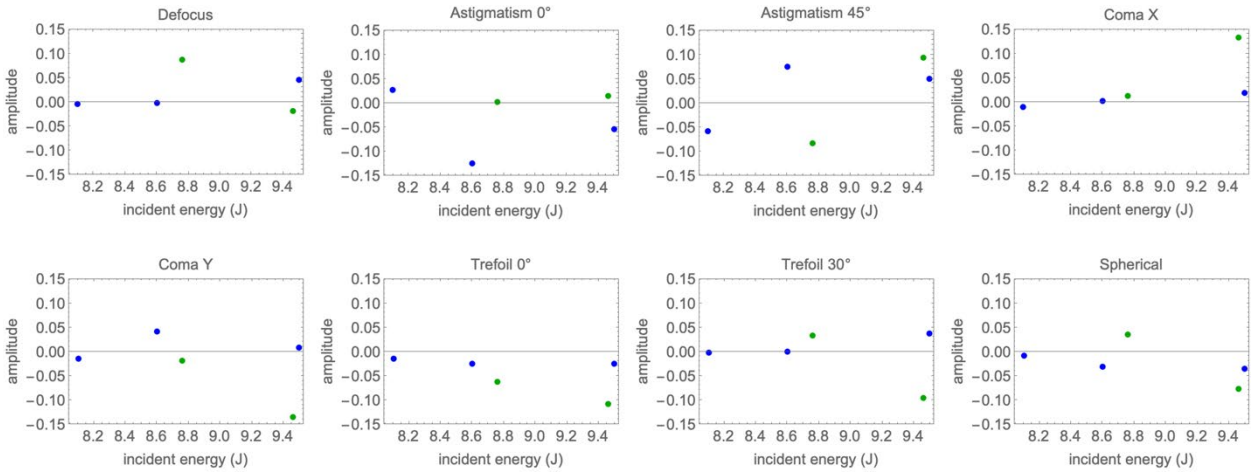

Figure 3-12. Zernike coefficient amplitudes (in waves) representing the aberrations induced on ellipsoidal SM shots (pre-shot aberrations subtracted). Blue points represent 2x magnification ellipsoids were used and green points represent 2.5x magnification ellipsoids were used.

3.2. High Intensity TNSA Experiments as Surrogate for LWFA Feasibility

The experimental results from the SM campaigns revealed some distortion to the reflected wavefront, which has implications for the focusability and intensity achievable. The measured aberrations shown in Figure 3-8 can be used to predict the degradation to the focal intensity, resulting in minor reductions in some cases or larger reductions up to 50% in others. While the fluctuations in these results is concerning, the conclusion made from these measurements is that high peak intensities can still be achieved in some cases. This would suggest that a LWFA stage following flat SMs would be plausible. In order to yield higher confidence in this conclusion, a campaign was designed to perform high-intensity, solid target experiments to drive Target Normal Sheath Acceleration (TNSA). This proton acceleration mechanism requires similarly high laser intensities and produces a proton spectrum that is sensitive to the on-target intensity that was achieved. By comparing TNSA experiments with and without the implementation of flat SMs, more certain conclusions can be made regarding the feasibility of using SMs and achieving high intensities.

3.2.1. Experiment Design

In this campaign, TNSA experiments using 25 μm copper foil targets were performed in two configurations. The first configuration used targets placed at the usual ZPW focus in the Chama target chamber. Laser and target alignment was performed using a through-focus imaging camera and a target side-on imaging camera paired with a PicoQuant laser probe. Detection of the TNSA protons was performed using a radiochromic film stack (alternating layers of radiochromic film and nickel filters, see recipe in Table 3-1). Additionally, the x-ray line emission near 8 keV from the copper target was measured using the CRITR diagnostic as a secondary metric to infer on-target intensities. Shots were performed near the 130 J level.

The second configuration inserts a flat SM into the focusing ZPW beam and shifts the copper foil target to the new focus. The SM and beam geometry was the same as implemented in the laser characterization campaign, which allowed the use of the same diagnostic cameras on the external diagnostic breadboard for laser/target alignment purposes. Shots were performed near the 160 J level,

higher than in the first configuration to compensate for the SM reflectance and produce a nearly 130 J energy on the TNSA target.

Table 3-1. Radiochromic film stack recipe used to measure TNSA protons

Layer #	Material	Breach Proton Energy
Filter	63 μm Kapton tape	
Filter	16 μm Al foil	
1	**HD-v2 film**	2.5 MeV
2	**HD-v2 film**	4.1 MeV
3	**HD-v2 film**	5.2 MeV
4	**HD-v2 film**	6.2 MeV
5	**HD-v2 film**	7.1 MeV
6	**HD-v2 film**	7.9 MeV
Filter	127 μm Ni foil	
7	**HD-v2 film**	11.6 MeV
Filter	127 μm Ni foil	
8	**HD-v2 film**	14.7 MeV
9	**EBT-3 film**	15.8 MeV
Filter	127 μm Ni foil	
10	**EBT-3 film**	18.9 MeV
Filter	127 μm Ni foil	
11	**EBT-3 film**	21.7 MeV
Filter	127 μm Ni foil	
12	**EBT-3 film**	24.3 MeV
Filter	127 μm Ni foil	
13	**EBT-3 film**	26.6 MeV
Filter	127 μm Ni foil	
14	**EBT-3 film**	28.8 MeV
Filter	254 μm Ni foil	
15	**EBT-3 film**	32.2 MeV
Filter	254 μm Ni foil	
16	**EBT-3 film**	35.4 MeV
Filter	254 μm Ni foil	
17	**EBT-3 film**	38.3 MeV
Filter	254 μm Ni foil	
18	**EBT-3 film**	41.1 MeV

3.2.2. *Experimental Results*

A total of 10 shots were performed as part of this campaign, with 5 shots that did not use SMs and 5 shots that did. Additionally, results from a prior TNSA campaign were used for additional non-SM reference data. The results presented below confirm the conclusion from the laser characterization experiments, namely that high peak intensities can still be achieved after reflection from a flat SM, but there are shot-to-shot fluctuations that make results less repeatable than desired.

- Figure 3-13 shows the maximum breach proton energy measured for all TNSA shots.
- Figure 3-14 presents the x-ray line brightness from the copper target measured by the CRITR spectrometer diagnostic, including the k-α, k-β, and He-α lines.

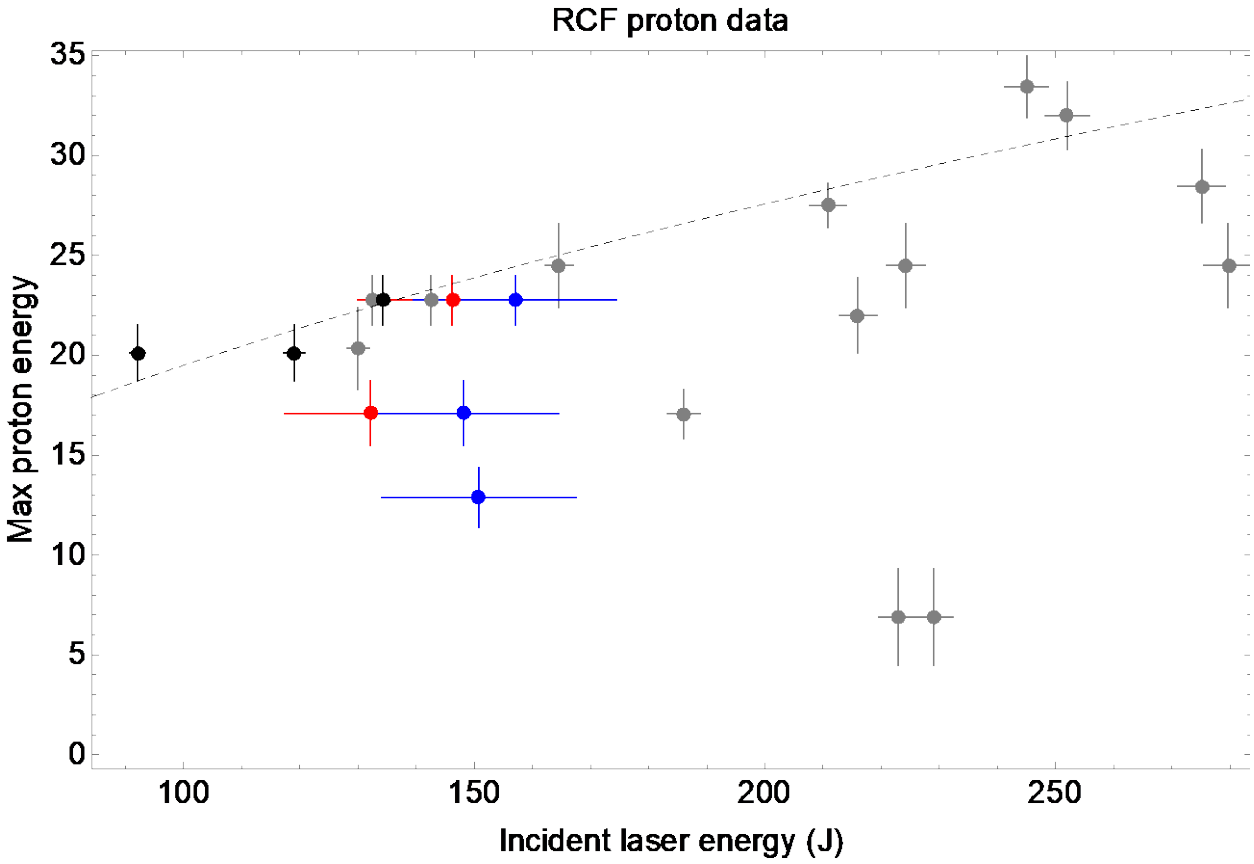

Figure 3-13. Max breach proton energies for all TNSA shots. Colors represent data from non-SM TNSA shots (black), silver-coated SM TNSA shots (red), dielectric-coated SM TNSA shots (blue), and non-SM TNSA shots from a prior campaign (gray). For SM shots, laser energies shown are incident on the SM, causing a somewhat reduced energy at the TNSA target. The dashed line scales as $E^{1/2}$, representing the expected scaling for TNSA proton energies.

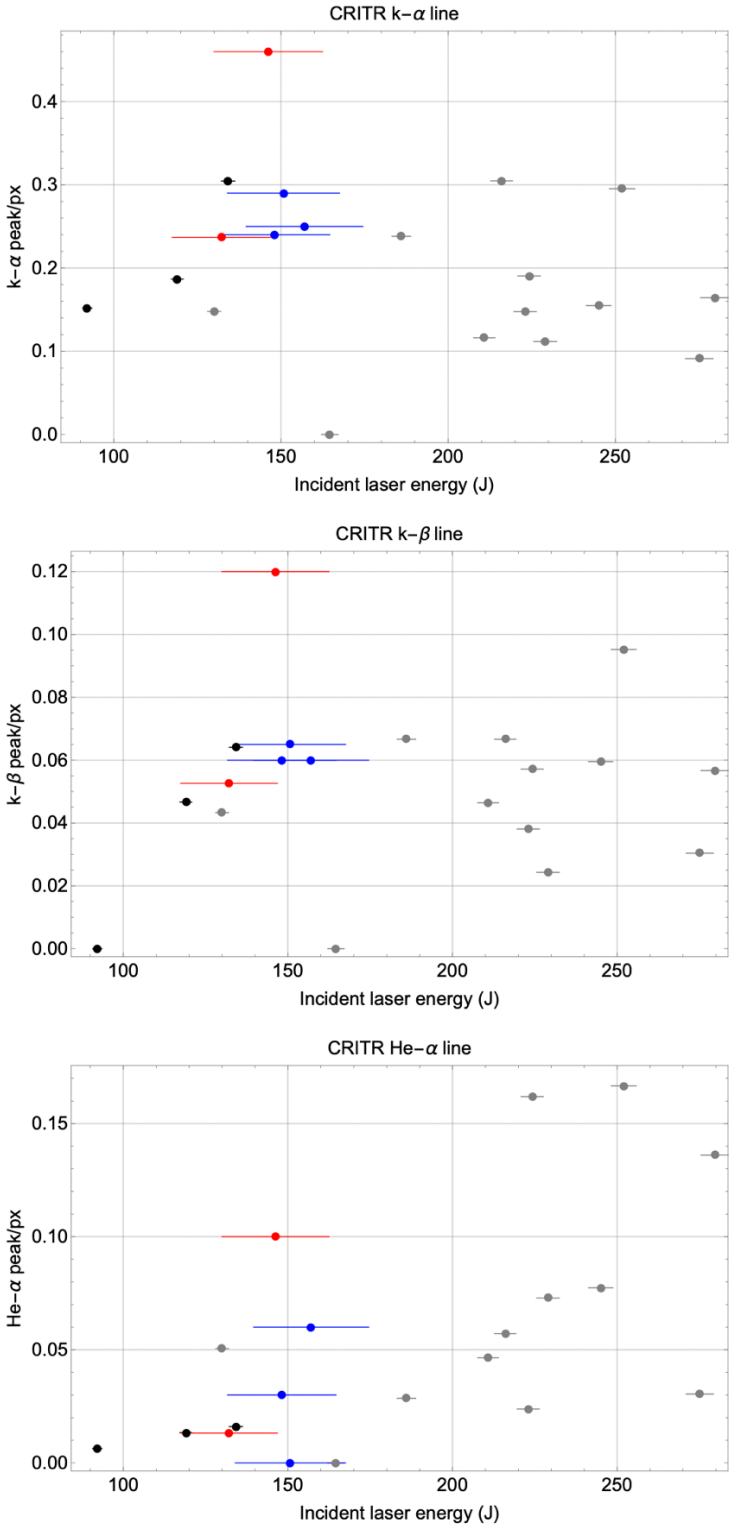

Figure 3-14. X-ray line brightness produced from copper foil targets and measured by the CRITR spectrometer diagnostic for all TNSA shots. Colors represent data from non-SM shots (black), silver-coated SM shots (red), dielectric-coated SM shots (blue), and non-SM shots from a prior campaign (gray). For SM shots, laser energies shown are incident on the SM, causing a somewhat reduced energy on the foil target.

3.3. ICEPIC Simulations of LWFA

The aberrations induced by reflection from SMs have been shown to be non-negligible based on direct laser characterization (see Fig. 3-8) as surrogates for LWFA. While the experimental infrastructure to directly perform LWFA experiments was not available in the first year of the LDRD project, an investigation into the sensitivity of LWFA to aberrations could be pursued via simulation. A collaboration with scientists from the Air Force Research Labs was established, and 3D particle-in-cell simulations were performed using the ICEPIC code. With this simulation package, the driving laser's electric field profile and spatial phase can be modified to realize the effects of aberrations on the LWFA process. Baseline simulations without aberrations were performed, and first attempts were made to apply aberrations that were consistent with those observed from laser characterization experiments.

3.3.1. Baseline LWFA Simulations with Flat Wavefront

Many of the LWFA simulations performed in the literature are performed in the "bubble" or "blowout" regime of LWFA that typically require ultrashort pulse lasers (<50 fs) such as those produced by Ti:Sapphire laser systems. This regime is convenient for simulation due to the relatively small spatial extent of the ultrashort laser pulse and the correspondingly small computational resources required to encompass this range. The first ICEPIC simulation performed was intended to replicate such simulations found in literature, with follow-up simulations gradually increasing the pulse duration toward the 500 fs duration of the ZPW laser. All of these simulations use a flat laser wavefront, representing a lack of aberrations and a transform-limited focal spot. Snapshots of the electron densities and energies generated by these simulations are displayed below:

- Figure 3-15 shows the electron densities observed at mid- and late times from an ICEPIC simulation using a 30 fs laser pulse and flat wavefront.
- Figure 3-16 shows the electron densities observed at late times from an ICEPIC simulation using a 133 fs laser pulse and flat wavefront.
- Figure 3-17 shows the electron densities observed at late times from an ICEPIC simulation using a 500 fs laser pulse and flat wavefront.

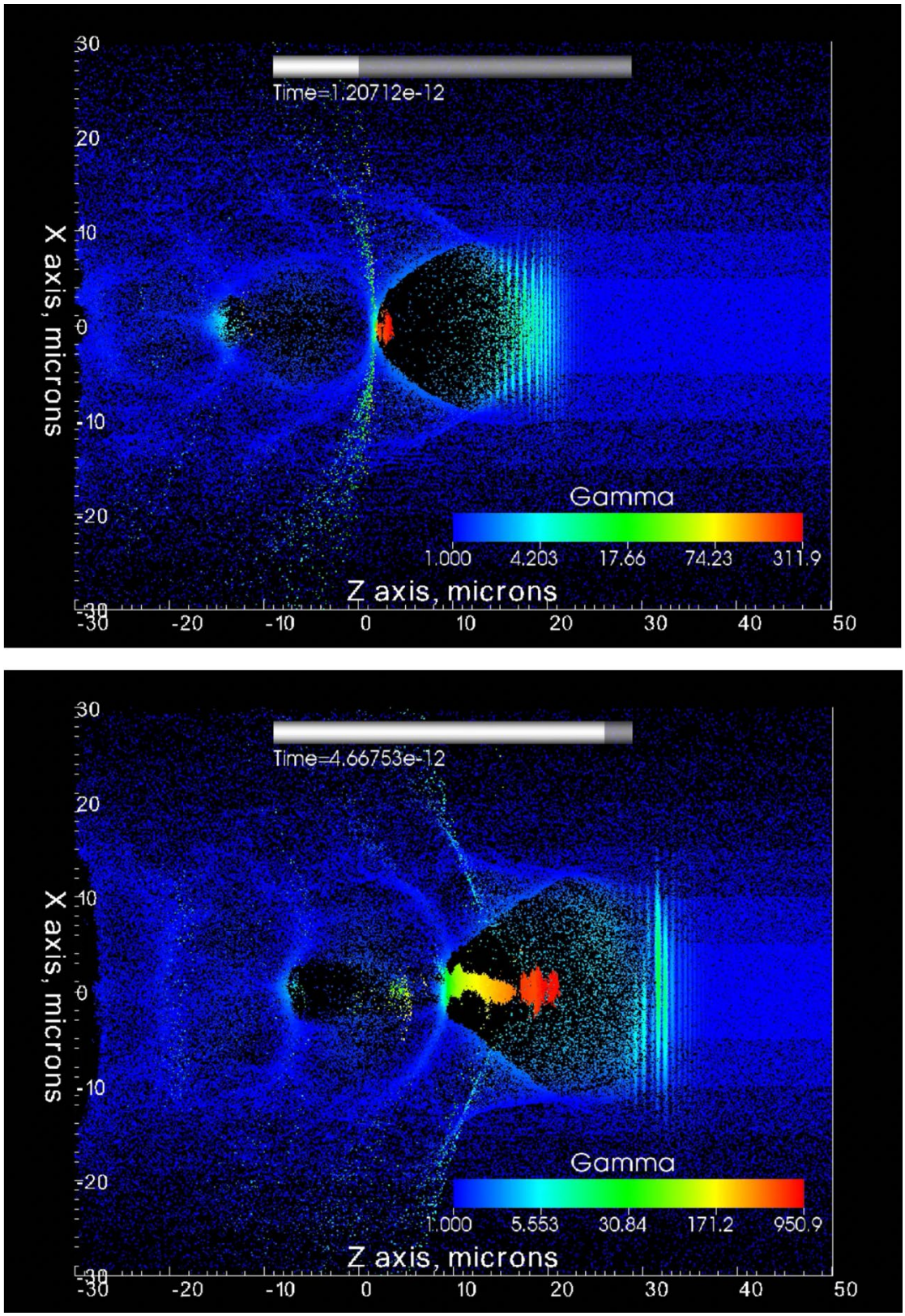

Figure 3-15. ICEPIC simulation results using a 30 fs laser pulse with flat wavefront. Mid- and late times within the same simulation are shown. Simulation parameters are as follows: τ = 30 fs, λ = 805 nm, w_0 = 13.6 μm, E = 1.51 J, I_{peak} = 1.6x10^{19} W/cm^2, n_p = 6.5x10^{18} cm^{-3}

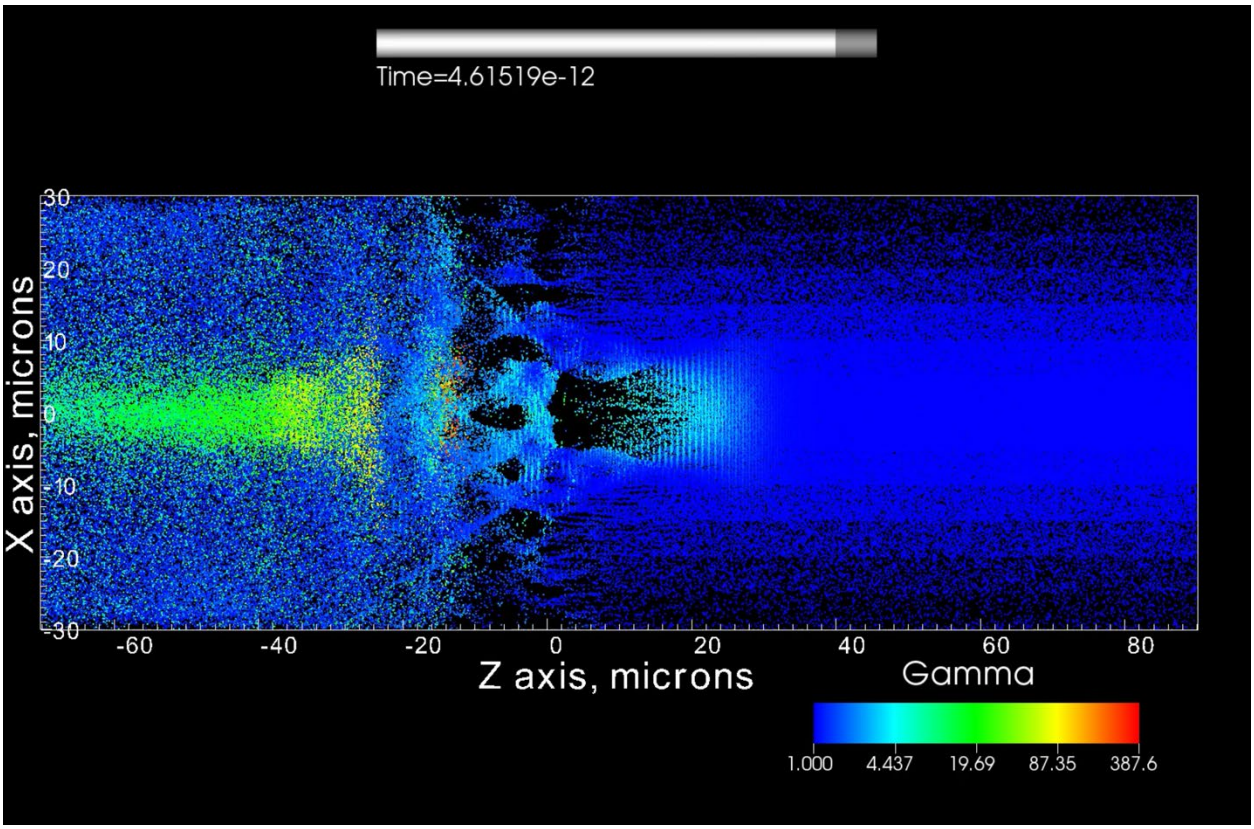

Figure 3-16. Late-time ICEPIC simulation result using a 133 fs laser pulse with flat wavefront. Simulation parameters are as follows:
τ = 133 fs, λ = 805 nm, w_0 = 13.6 μm, E = 6.7 J, I_{peak} = 1.6x10^{19} W/cm^2, n_p = 6.5x10^{18} cm^{-3}

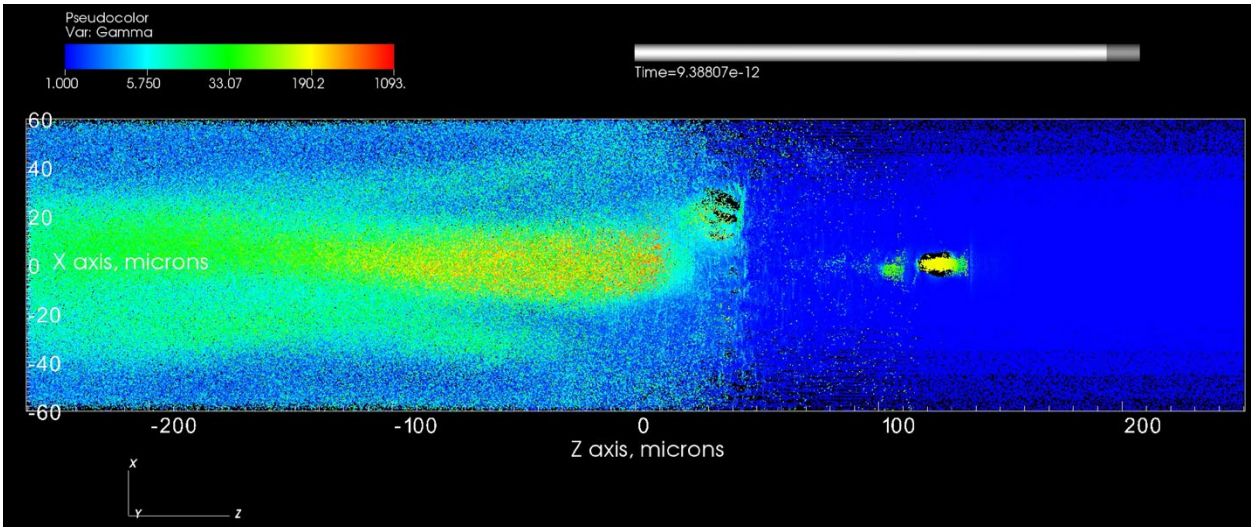

Figure 3-17. Late-time ICEPIC simulation result using a 500 fs laser pulse with flat wavefront. Simulation parameters are as follows:
τ = 500 fs, λ = 1054 nm, w_0 = 15 μm, E = 119 J, I_{peak} = 6.3x10^{19} W/cm^2, n_p = 1.0x10^{19} cm^{-3}

3.3.2. *LWFA Simulations with Aberrated Wavefronts*

Using representative aberration coefficients measured from the experiments described in section 3.1, the electric field amplitude and phase at the laser focus can be calculated through Fourier optics methods. Using this focal plane field description for the driving laser, ICEPIC simulations were performed to evaluate the effects of aberrations on the LWFA process. The results shown below provide an indication that aberrations have a substantial influence on the electron energies achievable, as well as their directionality given the transverse motion of the plasma wake as the simulation proceeds (see Figure 3-19).

- Figure 3-18 shows the transverse electric field amplitude and phase for the aberrated driving laser input for the ICEPIC simulation shown in Figure 3-18.
- Figure 3-19 shows the electron densities observed at mid- and late times from an ICEPIC simulation using a 100 fs laser pulse and aberrated wavefront consistent with the measurements described in section 3.1.

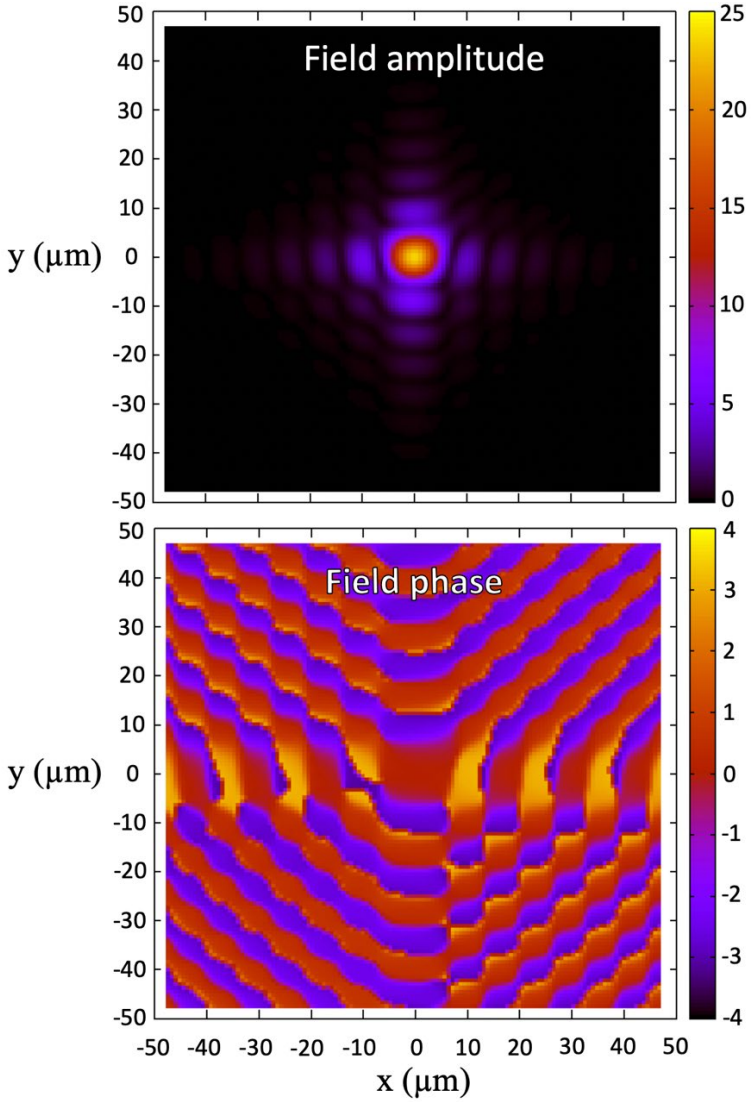

Figure 3-18. The electric field amplitude and phase used for the aberrated driving laser input for the ICEPIC simulation shown in Figure 3-18.

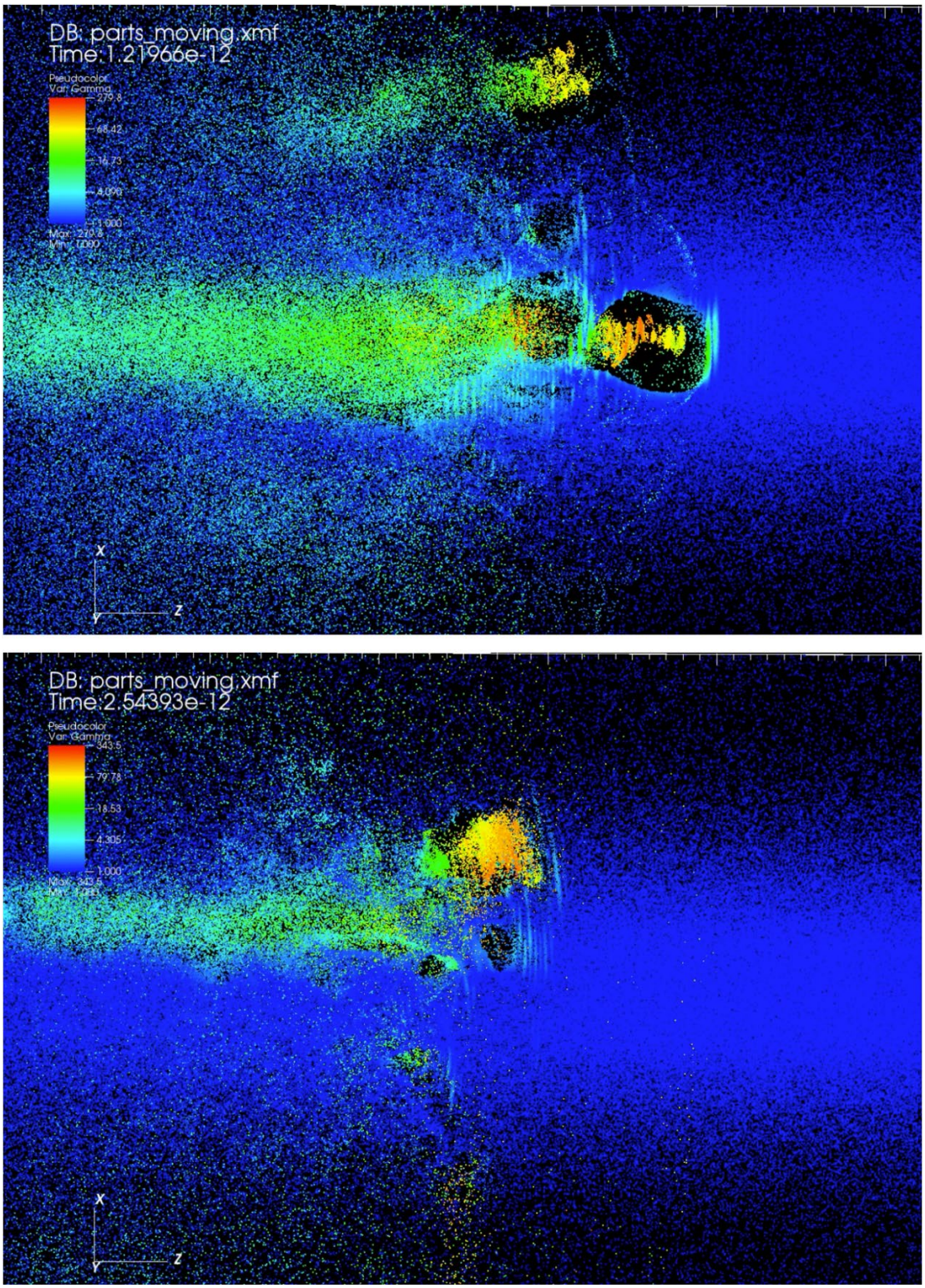

Figure 3-19. ICEPIC simulation results using a 100 fs laser pulse with an aberrated wavefront. Mid- and late times within the same simulation are shown. Simulation parameters are as follows: τ = 100 fs, λ = 1054 nm, w_0 = 13.6 μm, E = 5.08 J, I_{peak} = 1.64x10^{19} W/cm^2, n_p = 3.0x10^{19} cm^{-3}

4. CONCLUSIONS

4.1. Interpretation of Data and Summary of Accomplishments

In pursuit of developing a LWFA x-ray source for diagnostic applications on the Z Machine, designs were developed to describe the routing of the Z-Petawatt laser in the Z center section. The use of sacrificial mirrors was found to be necessary, so an offline investigation into the use of these mirrors was performed in the Chama target chamber. Three experiments were performed: 1) reflected laser characterization using flat SMs, 2) reflected laser characterization using ellipsoidal SMs, and 3) TNSA experiments performed with and without SMs as a surrogate for a LWFA platform.

The use of flat SMs had somewhat mixed results. The reflected laser characterization tests with flat SMs were energy-limited to avoid damage or distortions in the diagnostics. Within the applicable range of energies and the design fluences, SMs used below the threshold of plasma generation had the normal high reflectivity of the mirror which dropped significantly as the energy ramped up above the ignition threshold. Continued increases in energy led to reflectivities of around 80% (see Fig. 3-7), regardless if metallic or dielectric coatings, which is consistent with literature. With this in mind, higher energies were found to induce some level of on-shot aberration to the reflected laser (see Fig. 3-8). While many of the Zernike coefficients were found to vary in sign and magnitude, three coefficients were found to have consistent signs and some magnitude dependence on incident energy level: defocus, astigmatism 0, and coma X. All of these coefficients imply the generation of a curved plasma reflection surface that gets worse with increased energy, which could be due to hydrodynamic expansion from either a prepulse or the main pulse (see Fig. 3-9, which indicates a slow nanosecond-scale ramp before the main pulse). Pulse contrast improvements may thus mitigate the wavefront degradation. With all induced aberrations considered in the scenario as it exists, it is expected that the reflected beam will have reduced focal intensity after a sacrificial mirror than otherwise. That said, the worst contribution of any single Zernike term in the energy range studied was about 0.25 waves peak, which would generally be considered "diffraction-limited" in the absence of multiple combined aberrations. To clarify such uncertainty, subsequent comparison of laser-generated protons was needed (see section 3.2). Note that there could be wavefront pre-correction approaches to counteract the Zernike coefficients that appear to be consistent shot-to-shot. Even without pre-correction schemes, the amount of intensity reduction can vary. Based on the results from this study and the ICEPIC simulations of aberrated LWFA, it is expected that some amount of LWFA can indeed occur but with lower electron energies and some variation in the directionality of the electron/x-ray beams.

In LWFA, theory indicates that for the Z-Petawatt energy and pulse duration, driving the plasma with longer f/# focusing optics would benefit the LWFA process. For single shot experiments, the use of ellipsoidal SMs could accomplish this within a small chamber and without the need for long beam tubes. The laser characterizations performed in this study's ellipsoidal SM campaign were found to be limited to lower incidence energies. Precise alignment of the ellipsoids as well as requiring stringent quality specifications were found to be crucial to produce a reflected beam with low amplitude modulation – a requirement to transport the beam to diagnostics without damage to optical surfaces. While it is expected to be feasible to produce a suitable focal spot after high-energy reflection from an ellipsoidal SM, the laser characterizations performed in this study did not provide conclusive evidence of this.

While reflected laser characterizations can suggest the feasibility of strong performance in high intensity laser-target experiments, more confidence can be achieved by performing such experiments. TNSA experiments (see section 3.2) were performed with and without SM reflections before copper foil targets. Proton energies achieved without SMs provided a baseline for comparison, and the shots

performed with SMs were able to achieve comparable proton energies in 2 of the 5 shots performed (see Fig. 3-13). The small dataset does not make clear whether the proton signal variability in the SM cases is due to focal spot quality or degradation issues, target placement irregularities, or other shot-to-shot fluctuations. In fact, similar proton variability also appears (see Fig. 3-13) when the SM was not used. By comparison, the x-ray signals with an SM before the foil target seemed similar to or even stronger than those x-ray signals without an SM (see Fig. 3-14), which implies the any laser focal spot effects from the SM are not significant enough to impact the laser-matter interactions. It is important to note that performance was evaluated based on the incident energy on the sacrificial mirror. Evaluating on the basis of reflected energy, proton results recover slightly and X-ray results are clearly on-par or better than without mirror, which is important when considering the impact of wavefront distortions.

The ICEPIC simulations, although not fully exploring anticipated performance for Z-Petawatt parameters with the measured wavefront distortions, indicate that Laser-Wakefield Acceleration is plausible with sacrificial mirrors. The results with modified wavefront indicate electron energies in excess of 35 MeV ($\gamma > 70$) for a 100 fs laser pulse, which may further increase for longer pulses. This should be sufficient to generate hard X-rays.

In general, the arguable irreproducibility and poor shot statistics cause concern for the LWFA x-ray diagnostic application for precious Z shots, particularly if this diagnostic is considered critical for the goals of the experiment. Reproducibility might improve through further investigations (improved target placement methods and shot statistics) and with laser upgrades, such as improvements to pulse contrast, pulse compression, and removal of chromatic aberration.

4.2. Path Forward

The LDRD project ended in January 2022 as a result of the principal investigator transitioning away from Sandia. If this project were to be resumed, the project plan in section 2.2 describes the path forward to develop the LWFA platform and mature it to a point where it could be used on the Z Machine. Further investigations into SMs could be warranted to improve the reliability of achieving a high-quality focal spot after reflection. Upgrades to the Z-Petawatt laser parameters and quality would likely aid in this effort. An infrastructural investment into reactivating the Z-Petawatt Final Optics Assembly is required to deliver the Z-Petawatt laser into the center section and perform the necessary beam routing for the diagnostic system's horizontal line of sight.

REFERENCES

[1] Albert et al., Phys. Plasmas **25**, 056706 (2018).

[2] Lemos et al., Phys. Plasmas **26**, 083110 (2019).

[3] Dagel et al., SAND Report SAND2016-11762

[4] Kneip et al., Appl. Phys. Lett. **99**, 093701 (2011).

[5] Wenz et al., Nat. Comm. **6**, 7568 (2015).

[6] Suggit et al., Nat. Comm. **3**, 1224 (2012).

[7] Comley et al., Phys. Rev. Lett. **110**, 115501 (2013).

[8] Schollmeier et al., SAND Report SAND2013-7201

[9] Nakatsutsumi et al., Opt. Lett. **35**, 2314-2316 (2010).

[10] Chen, Stephen. "Operation Z Machine: China's next Big Weapon in the ..." South China Morning Post, 12 Dec. 2018.

[11] Lash et al., SAND Report SAND2017-0900PE

[12] Rambo et al., Proc. SPIE **10014**, 100140Z (2016).

[13] Schollmeier et al., Rev. Sci. Instrum. **89**, 10F102 (2018).

[14] McBride et al., Phys. Rev. Lett. **109**, 135004 (2012).

[15] Awe et al., Phys. Rev. Lett. **116**, 065001 (2016).

[16] Awe et al., Phys. Plasmas **21**, 056303 (2014).

[17] Sinars et al., Phys. Plasmas **27**, 070501 (2020).

[18] McBride et al., Phys. Plasmas **20**, 056309 (2013).

[19] Rovang et al., PPPS-2001, 1012-1015 vol. 2. (2001).

[20] Shelkovenko et al., Phys. Plasmas **23**, 103303 (2016).

[21] Platts et al., 10th IEEE Intl. P.P. Conf. **2**, 892-896 (1995).

[22] Conversations with Clayton Myers, Jan 2020.

[23] Gonsalves et al., Phys. Rev. Lett. **122**, 084801 (2019).

[24] Mangles et al., Plas. Phys. and Cont. Fus. **48**, 12B (2006).

[25] Sinars presentation, ARPE-E Workshop (2013).

[26] Sinars et al., Applied Optics **42** (19), 4059-4071 (2003).

[27] Endrizzi, Nuc. Inst. and Meth. in Phys. Res. A, **878**, 88-98 (2018).

[28] Fourmaux et al., Proc. of SPIE **8412**, 841211-1 (2012).

[29] Kieffer et al., SPIE Newsroom (2016); doi:10.1117/2.1201610.006713

[30] Kedesey, American Minerologist 39 (9-10): 750-760 (1954).

[31] Lee et al., Mat. Res. Bulletin **37**, 555-562 (2002).

[32] Kaito et al., J. Phys. Chem. C **118**, 8481-8490 (2014).

DISTRIBUTION

Email—Internal

Name	Org.	Sandia Email Address
Benjamin Galloway	01682	brgallo@sandia.gov
Patrick Rambo	01682	prambo@sandia.gov
Matthias Geissel	01682	mgeisse@sandia.gov
Mark Kimmel	01682	mwkimme@sandia.gov
Jeffrey Kellogg	01691	jwkello@sandia.gov
Patrick Knapp	01683	pfknapp@sandia.gov
Richard Harrison	06753	rkharri@sandia.gov
Kyle Thompson	01529	krthomp@sandia.gov
Amber Dagel	05228	aldagel@sandia.gov
John Porter	01682	jlporte@sandia.gov
Greg Rochau	01680	garocha@sandia.gov
Chris Seagle	01646	ctseagl@sandia.gov
Luke Shulenberger	01641	lshulen@sandia.gov
Matt Burger	01380	mjburge@sandia.gov
Technical Library	01977	sanddocs@sandia.gov

Email—External [redacted]

Name	Company Email Address	Company Name
Jennifer Elle	jennifer.elle.1@us.af.mil	AFRL
Travis Garrett	travis.garrett.2@us.af.mil	AFRL

Hardcopy—Internal

Number of Copies	Name	Org.	Mailstop
1	Benjamin Galloway	01682	1192
1	Matthias Geissel	01682	1192
1	Mark Kimmel	01682	1192
1	John Porter	01682	1192
1	Patrick Rambo	01682	1192

This page left blank

This page left blank

Sandia National Laboratories

Sandia National Laboratories is a multimission laboratory managed and operated by National Technology & Engineering Solutions of Sandia LLC, a wholly owned subsidiary of Honeywell International Inc. for the U.S. Department of Energy's National Nuclear Security Administration under contract DE-NA0003525.